Ionosphere plasma bubbles and density variations induced by pre-earthquake rock currents and associated surface charges

C. L. Kuo,[1,2] J. D. Huba,[3] G. Joyce,[4] and L. C. Lee[1,2]

Received 7 March 2011; revised 1 July 2011; accepted 25 July 2011; published 20 October 2011.

[1] Recent ionospheric observations indicate that the total electron content (TEC) may anomalously decrease or increase up to 5–20% before the occurrence of big earthquakes. The ionospheric density variations can be caused by earth surface charges/currents produced from electric currents associated with the stressed rock. We formulate a coupling model for the stressed rock-Earth surface charges-atmosphere-ionosphere system. The stressed-rock acts as the dynamo to provide the currents for the coupling system. The electric fields and currents in the atmosphere and the lower boundary of ionosphere are obtained by solving the current continuity equation, $\nabla \cdot \boldsymbol{J} = 0$, where $\boldsymbol{J}$ is the current density. A three-dimensional ionosphere simulation code is then used to study the ionospheric dynamics based on the obtained electric fields and currents. The simulation results show that a current density J_{rock} = 0.2–10 μA/m^2 in an earthquake fault zone is required to cause daytime TEC variations of 2–25%. The simulation results also show that a current density J_{rock} = 0.01–1 μA/m^2 can lead to nighttime TEC variations of 1–30% as well as the formation of a nighttime plasma bubble (equatorial spread F) extending over the whole magnetic flux tube containing the earthquake epicenter. We suggest that observations of daytime and nighttime TEC variations and a nighttime plasma bubble within the affected region can be used as precursors for earthquake prediction.

Citation: Kuo, C. L., J. D. Huba, G. Joyce, and L. C. Lee (2011), Ionosphere plasma bubbles and density variations induced by pre-earthquake rock currents and associated surface charges, *J. Geophys. Res.*, *116*, A10317, doi:10.1029/2011JA016628.

1. Introduction

[2] Earthquake precursors can be used for earthquake prediction [*Scholz et al.*, 1973; *Geller*, 1997; *Toutain and Baubron*, 1999; *Kanamori*, 2003; *Bolt*, 2004] to reduce the loss of resources and human lives. As early as the 1960 Chile earthquake (largest earthquake recorded), the critical frequency of the F2 layer (f_o F2) on 20 May before main shock were slightly below its median value for a few hours in a period of quiet geomagnetic activities [*Foppiano et al.*, 2008]. For the 1964 Alaska earthquake, scientists also found magnetic disturbances and ionospheric irregularities in the magnetometer and ionosonde data before the main shock of the 1964 Alaska earthquake [*Moore*, 1964; *Davies and Baker*, 1965]. Additional pre-earthquake ionospheric signatures have been reported that include ground and satellite-measured electromagnetic perturbations [*Park et al.*, 1993; *Parrot et al.*, 1993; *Bhattacharya et al.*, 2009], ionosonde-recorded variations of f_o F2 [*Liu et al.*, 2000; *Chuo et al.*, 2001; *Silina et al.*, 2001], and GPS-measured TEC [*Liu et al.*, 2001; *Zhao et al.*, 2008; *Liu et al.*, 2009]. These findings suggest that an electrical seismic-ionosphere coupling exists [*Pulinets et al.*, 2000; *Pulinets and Boyarchuk*, 2004].

[3] Ionosphere density variations caused by pre-earthquake surface charges and electric field have been reported based on a simplified model [*Pulinets et al.*, 2000, 2003; *Pulinets and Boyarchuk*, 2004]. The simulation domain is limited to a local hemisphere region with an altitude between 200 and 700 km is considered in the model. The temperatures of neutrals, ions and electrons are fixed to 800 K. Therefore, the variation of daytime electron temperature and nighttime plasma bubble development cannot be obtained using this simplified model.

[4] In this report we use the comprehensive Naval Research Laboratory (NRL) ionosphere model SAMI3 [*Huba et al.*, 2008] to study the impact of an earthquake generated electric field on the ionosphere. SAMI3 simulates the temporal and spatial evolution of seven ion species (H^+, He^+, N^+, O^+, N_2^+, NO_2^+ and O_2^+) over the entire magnetic flux tube in both hemispheres. The density and velocity equations are solved for all ion species; the ion temperature equation is solved for H^+, He^+, and O^+ as well as the electron temperature equation. The latitude range of the simulation domain is ±30°, the longitude range is 8°, and the range of magnetic apex heights is 85 to 2400 km. The grid is (*nz*, *nf*, *nl*) = (101, 156, 70), where *nz* is the number

[1]Institute of Space Science, National Central University, Jhongli, Taiwan.
[2]Department of Physics, National Cheng Kung University, Tainan, Taiwan.
[3]Plasma Physics Division, Naval Research Laboratory, Washington, D. C., USA.
[4]Icarus Research, Inc., Bethesda, Maryland, USA.

0148-0227/11/2011JA016628

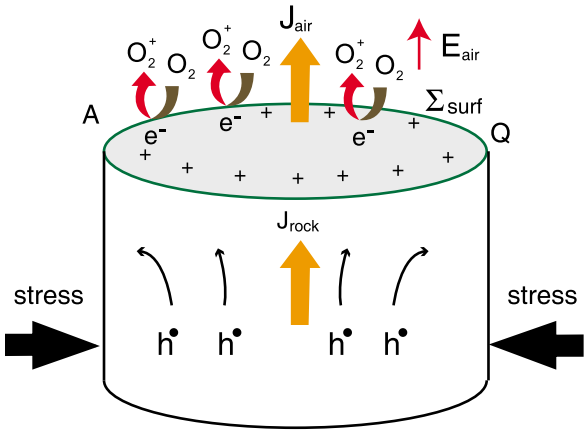

Figure 1. As rocks are subjected to stress force in the earthquake preparation region, the deformation of lattice structure in rocks can produce electronic charge carriers (positive holes, $h^{\bullet}$) and electric currents (J_{rock}). The positive holes diffuse from the highly stressed region into the unstressed region, repel each other electrostatically, and push toward the rock surface. The field-ionization ($O_2 \rightarrow O_2^+ + e^-$) occurring at the surface, in particular at sharp points, can produce the O_2^+ ions. The surface charge density Σ_{surf} and total charge amount Q are accumulated by positive charges from the rock surface and O_2^+ ions in the air. The upward electric field $\boldsymbol{E}_{\rm air}$ associated with the positive surface charges will drive the upward current J_{air}.

grid points along the magnetic field, *nf* the number in altitude and *nl* the number in longitude. Thus, we are able to overcome the limitations of a simplified model and determine the complete ionospheric response to a pre-earthquake electric field. It is found that the presence of surface charges and electric field can lead to TEC variations and trigger the formation of plasma bubble.

[5] In section 2, we describe the stress-activated electric currents in rocks [*Freund*, 2000, 2002; *Freund and Sornette*, 2007; *Freund et al.*, 2009; *Freund*, 2010] and derive the surface charge density and electric field at the ground-to-atmosphere interface. In section 3, we use the current continuity equation to calculate the current density and electric fields in the atmosphere, and we use the 3D SAMI3 model to examine the ionosphere dynamics. In sections 4 and 5, we show the daytime and nighttime results of the ionospheric dynamics, respectively.

2. Hole Charge Carriers From Stressed Rock and Accumulated Charges Over Earth Surface

[6] Laboratory experiments [*Freund*, 2000, 2002; *Freund and Sornette*, 2007; *Freund et al.*, 2009; *Freund*, 2010] demonstrated that, as rocks are subjected to stress, rocks can activate positive holes ($h^{\bullet}$) as charge carriers and generate electric currents along the stress-gradient direction with current density $\boldsymbol{J}_{\rm rock}$, as illustrated in Figure 1. The hole charge carriers pre-exist in unstressed rocks in a dormant electrically inactive state as peroxy links, $O_3Si\text{-}OO\text{-}SiO_3$, where two O^- are tightly bound together. Under stress, dislocations in lattice sweep through the mineral grains causing the peroxy link to break. The broken peroxy link acts as electron receptor: it takes the electron (e′) and holds on to it, while a structure unit $[SiO_4]^{4-}$ donates the electron, becomes $[SiO_4]^{3-}$, and thereby turns into a positive hole, symbolized by $h^{\bullet}$. The electron becomes trapped at the broken peroxy link while the mobile positive holes can propagate by electrons hopping from O^{2-} to O^-. The $h^{\bullet}$ outflow from the stressed rock has two consequences: (1) it sets up a potential difference, which causes the unstressed rock to become positively charged relative to the stressed rock; (2) the mobile $h^{\bullet}$ charge carriers inside the unstressed rock repel each other electrostatically and will be pushed toward the surface.

[7] The accumulation of positive hole charge carriers $h^{\bullet}$ at the surface produces a positive surface charges as shown in Figure 1. The microscopic high electric field at sharp edge of rock surface may cause air molecules to be ionized. One of those processes is the field ionization of air molecules, ($O_2 \rightarrow O_2^+ + e^-$), producing O_2^+ ions and electrons. The delivery of these electrons to the rock surface may cause more $h^{\bullet}$ influx from the bulk rock. The effect of the field ionization of air molecules can be seen as to move some of the positive surface charges to the air with O_2^+ ions across the air-rock interface [*Freund*, 2010].

[8] Let Σ_{surf} be the surface charge density, which consists of the contribution of positive charges from the rock surface and O_2^+ ions in the air. The associated electric field $\boldsymbol{E}_{air}$ can be written as

$$\boldsymbol{E}_{air} = \left(\Sigma_{surf}/\varepsilon_0\right)\hat{z}, \tag{1}$$

where $\hat{z}$ is the unit vector in the vertical direction, and ε_0 is the electric permittivity of free space. Due to the finite air conductivity, σ_{air}, the electric field will drive an upward current density,

$$\boldsymbol{J}_{air} = \sigma_{air}\boldsymbol{E}_{air}. \tag{2}$$

Let A be the surface area of the stressed rock, and $Q = A\Sigma_{surf}$ be the total surface charges above the rock. From equations (1) and (2), the total surface charges of stressed rock can be expressed as

$$Q = A\Sigma_{surf} = AJ_{air}(\varepsilon_0/\sigma_{air}). \tag{3}$$

The time variation of Q can be written as

$$dQ/dt = AJ_{rock} - AJ_{air} = AJ_{rock} - \sigma_{air}Q/\varepsilon_0, \tag{4}$$

The background air conductivity σ_0 is caused by the finite mobility (μ_+ and μ_-) of positive ions (n_{+0}) and negative ions (n_{-0}), which can be produced by various processes, including air ionizations by cosmic rays, radioactivity gases and radioactivity substances in the soil [e.g., *Rycroft et al.*, 2008]. Hence, $\sigma_0 = q_+\mu_+n_{+0} + q_-\mu_-n_{-0}$ where $n_{+0} = n_{-0} = 2.7 \times 10^8$ m^{-3}, positive ion mobility $\mu_+ = 2.5 \times 10^{-4}$ V m^2 s^{-1}, negative ion mobility $\mu_- = 2.2 \times 10^{-4}$ V m^2 s^{-1} [e.g., *Riousset et al.*, 2010] and hence $\sigma_0 \sim 2 \times 10^{-14}$ Sm^{-1}. If we ignore the conductivity caused by the stress-induced surface positive charge carriers, the analytic solution for the total surface charges Q in equation (4) can be obtained from

$$Q = Q_0\left(1 - e^{-t/\tau_0}\right), \tag{5}$$

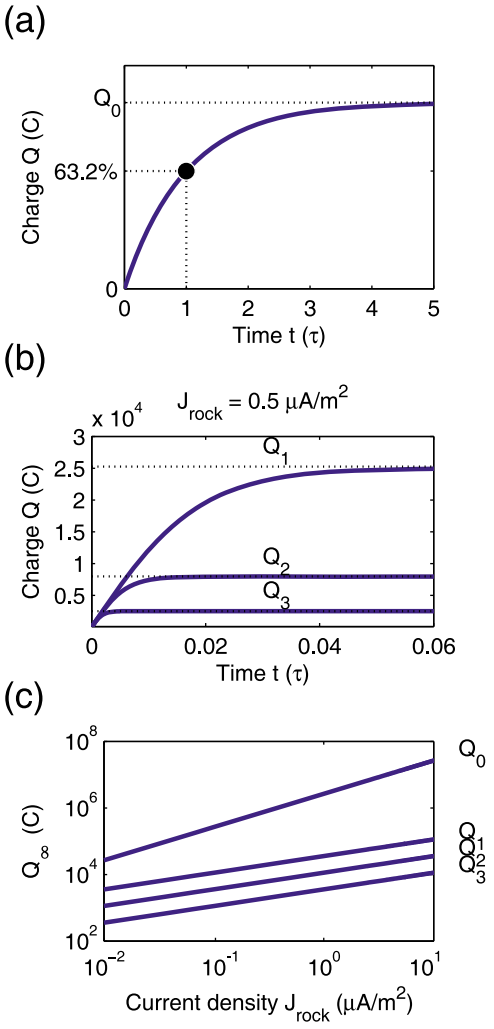

Figure 2. (a) The total surface charge Q as a function of charging time t, $Q = Q_0(1 - e^{-t/\tau_0})$, where $Q_0 = AJ_{rock}\,\tau_0$ is the asymptotic value of Q as $t \to \infty$ and $\tau_0 = \varepsilon_0/\sigma_0$(~440 s) near ground. (b) The numerical solution of surface charge $Q(t)$, for $A = 200 \times 30$ km^2, $I_{\rm rock} = 3 \times 10^3$ A, $J_{\rm rock} = 0.5$ μA/m^2 and $h = 1000$ m, 100 m and 10 m. The corresponding asymptotic total charge Q_∞ is $Q_1 = 2.5 \times 10^4$ C for $h = 1000$ m, $Q_2 = 8 \times 10^3$ C for $h = 100$ m, and $Q_3 = 2.5 \times 10^3$ C for $h = 10$ m. (c) The asymptotic total charge Q_∞ for Q_0, Q_1, Q_2, Q_3 as a function of current density J_{rock}.

where $\tau_0 = \varepsilon_0/\sigma_0$ and

$$Q_0 = AJ_{rock}\tau_0 = AJ_{rock}(\varepsilon_0/\sigma_0). \quad (6)$$

Figure 2a shows Q as a function of time. Let the asymptotic value of total charge be Q_∞. When Q reaches its asymptotic value $Q_\infty = Q_0$, the output total current $AJ_{\rm air}$ into atmosphere equals to input total current $I_{\rm rock} = AJ_{\rm rock}$ from rock, since $dQ/dt = 0$. In equation (5) and Figure 2a, τ_0 is the characteristic time for the build-up of surface charges to reach 63.2% of Q_0. *Freund et al.* [2009] have demonstrated in stressed rock experiments that a positive ion current of 10–25 nA is present over an area of collector plate 200 cm^2, corresponding to a current density $J_{\rm rock} \sim 0.5$–1.25 μA/m^2. Of course, the stressed-induced current density J_{rock} in the earthquake fault region may depend on the stress magnitude, stress gradient and other factors. With an earthquake plate area $A = 200 \times 30$ km^2, $J_{\rm rock} = 0.5$ μA/m^2 and $\sigma_0 = 2 \times 10^{-14}$ Sm^{-1}, we obtain $Q_0 = 1.3 \times 10^6$ C and $E_{\rm air} = 2.4 \times 10^7$ Vm^{-1}, greater than the threshold of required E field for air ionization (~3×10^6 Vm^{-1} near ground). In order to ionize the air, the E field does not have to extend over large distances. It is enough if an E field of such a magnitude exists on a microscopic scale, at the ground-to-air interface. The presence of these charges and electric field will modify the air conductivity and cause the air ionizations.

[9] We assume for illustration purpose that most of the stress-induced surface charges react with neutral gas molecules to produce molecular ions with a density n_{+1}, and these ions are contained in an air column with area A and height h. We then have $n_{+1} \approx Q/(eAh)$, where e is the magnitude of an electron charge. The extra positive ions will provide an additional conductivity $\sigma_1 = en_{+1}\mu_+$. Therefore,

$$\sigma_{air} = \sigma_0 + \sigma_1 = \sigma_0 + \mu_+ Q/(Ah). \quad (7)$$

Inserting $\sigma_{\rm air}$ into equation (4), we have

$$dQ/dt = AJ_{rock} - Q[\sigma_0 + \mu_+ Q/(Ah)]/\varepsilon_0. \quad (8)$$

As $dQ/dt = 0$, we have $Q = Q_\infty$, and

$$\mu_+/(Ah)Q_\infty^2 + A\sigma_0 Q_\infty - \varepsilon_0 I_{rock} = 0. \quad (9)$$

The above quadratic equation can be easily solved analytically. If $\sigma_0 \ll \sigma_1$, we have

$$Q_\infty = A\sqrt{\varepsilon_0 h J_{rock}/\mu_+}. \quad (10)$$

In Figure 2b, we plot the solution of equation (8), $Q(t)$, for $A = 200 \times 30$ km^2, $I_{\rm rock} = 3 \times 10^3$ A, $J_{\rm rock} = 0.5$ μA/m^2 and $h = 1000$ m, 100 m and 10 m. The asymptotic total charge Q_∞ is equal to $Q_1 = 2.5 \times 10^4$ C for $h = 1000$ m, $Q_2 = 8 \times 10^3$ C for $h = 100$ m, and $Q_3 = 2.5 \times 10^3$ C for $h = 10$ m. In Figure 2c, we plot Q_∞ for Q_0, Q_1, Q_2 and Q_3 as a function of $J_{\rm rock}$ for $A = 200 \times 30$ km^2. Note that Q_1, Q_2 and Q_3 are much smaller than Q_0.

[10] In short, the stressed rock acts as the dynamo (battery) to drive currents for the rock-surface charge-atmosphere-ionosphere coupling system to be furthered studied in the next sections. The pre-earthquake radon emanation may provide air ionizations, leading to the presence of both positive and negative ions in the air and enhance the air conductivity. However, it is unlikely that radon emanation can act as a dynamo to continuously maintain the required currents to drive the coupling system.

3. Electrical Coupling Between Ionosphere and Surface Charges in the Earthquake Fault Zone

[11] For simplicity, we assume that the earthquake fault zone has a length $a = 200$ km and a width $b = 30$ km. The surface charge density distribution over the fault zone can be expressed as

$$\Sigma_{surf}(x,y) = \frac{\Sigma_0}{4}\left[1 + \cos\frac{\pi(x - x_0)}{a}\right]\left[1 + \cos\frac{\pi(y - y_0)}{b}\right]. \quad (11)$$

where x and y are north-south and east-west directions; x_0 and y_0 are the geometric center of the fault zone; total surface charges Q_0 is calculated by $\int\int \Sigma_0(x, y)dxdy$ =

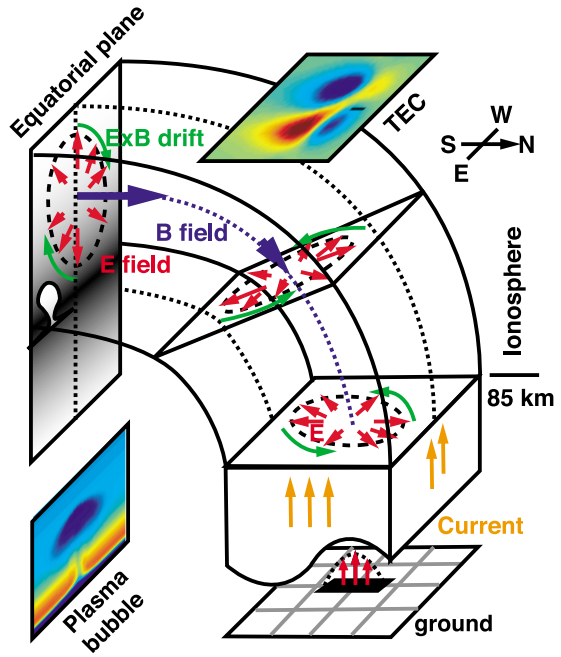

Figure 3. A sketch of electric coupling between the ionosphere and surface charges in the earthquake fault zone. The vertical surface electric field (red arrows) from surface current density $J_{\rm rock}$ over a fault zone drives the current (orange arrows) in the atmosphere and the electric field $\mathbf{E}_{z=85}$ at the bottom of the ionosphere at an altitude of 85 km. The electric field causes the $\boldsymbol{E} \times \boldsymbol{B}$ motion (green arrows) of ionosphere plasma leading to the formation of plasma vortex and TEC variations in the ionosphere. The external electric field also leads to an upward motion in the equatorial plane east of surface charge region and can trigger the formation of nighttime plasma bubbles.

$\sum_0 ab = \sum_0 A$, where $A = ab$ is the effective stressed area of the earthquake fault zone. The ground upward electric field is given by $E_{\rm air} = \sum_{surf}/\varepsilon_0$. Note that if positive hole charge carriers are generated along a fault, they have the capability to spread out laterally, affecting a much wider region than just along the fault line.

[12] The external electric field over an earthquake fault region was solved using the current continuity equation [*Tzur and Roble*, 1985]. The numerical domain is a three dimensional Cartesian coordinate system (x, y, z) where x and y are east/west and north/south directions in the horizontal plane of Earth ($-400 \le x \le 400$ km, $-600 \le y \le 600$ km) and z is the altitude, $0 < z < 100$ km. We assume the magnetic field is parallel to z-direction, and horizontally stratified medium (i.e., conductivity is only a function of altitude z). The current continuity equation can be written in terms of the electric potential (Φ) equation as

$$\begin{aligned}\nabla \cdot \boldsymbol{J} &= \frac{\partial}{\partial x}\left(\sigma_p \boldsymbol{E}_x\right) + \frac{\partial}{\partial y}\left(\sigma_p \boldsymbol{E}_y\right) + \frac{\partial}{\partial z}\left(\sigma_\parallel \boldsymbol{E}_z\right) \\ &= \frac{\partial}{\partial x}\left(\sigma_p \frac{\partial \Phi}{\partial x}\right) + \frac{\partial}{\partial y}\left(\sigma_p \frac{\partial \Phi}{\partial y}\right) + \frac{\partial}{\partial z}\left(\sigma_\parallel \frac{\partial \Phi}{\partial z}\right). \\ &= 0\end{aligned} \tag{12}$$

where $\sigma_\parallel$ is the conductivity along the magnetic field, and σ_p is the conductivity perpendicular to the magnetic field; $\boldsymbol{E}_x$, $\boldsymbol{E}_y$ and $\boldsymbol{E}_z$ are the electric fields in x-, y- and z-direction. Equation (12) is solved using the successive over-relaxation method adapted from MUDPACK package (http://www.cisl.ucar.edu/css/software/mudpack/) with the upper ionospheric boundary condition, $\frac{\partial J_\parallel}{\partial z} = 0$ [*Tzur and Roble*, 1985]. The current along the magnetic field is continuous and flows into the ionosphere. The use of upper boundary condition $E_\parallel = 0$, which implies $J_\parallel = 0$, leads to a much higher perpendicular electric field at z = 85 km. The assumption $J_\parallel = 0$ means that no current flows into the ionosphere, and upward current flows outwardly in the horizontal plane below the boundary at z = 85 km. The accumulated current will enhance the magnitude of electric field because $\boldsymbol{J} = \sigma \boldsymbol{E}$.

[13] The conductivity profile below 100 km is obtained from an empirical mode [*Cole and Pierce*, 1965]. For the altitude range of lower atmosphere, $0 \le z \le z_1$ where z_1 = 50 km (daytime) and 65 km (nighttime), the conductivities are isotropic and given by $\sigma_\parallel = \sigma_p = \sigma_{z=0} e^{z/h}$ where the conductivity at $z = 0$ is $\sigma_{z=0} = 2 \times 10^{-13}$ Sm^{-1}. The scale height of isotropic conductivity h is 6.5 km. For the upper atmosphere, $z_1 \le z \le z_2$ where z_2 is 100 km, the conductivities become anisotropic and are given by $\sigma_\parallel = \sigma_{z=z_1} e^{(z-z_1)/h_\parallel}$ and $\sigma_p = \sigma_{z=z_1} e^{(z-z_1)/h_p}$ where $\sigma_{z=z_1} = \sigma_{z=0} e^{z_1/h}$. The scale heights for parallel conductivity ($h_\parallel$) and Pedersen conductivity (h_p) are 3 km and 4.5 km, respectively.

[14] The conductivity profile used in our model is similar to the conductivity profile by *Rycroft et al.* [2008], except the value near the Earth surface. The conductivity near the ground is 2×10^{-13} S/m, which is higher than the conductivity 2×10^{-14} S/m in work by *Rycroft et al.* [2008], to partially include the contribution from molecule ionization caused by rock currents (the σ_1 term). The conductivity at 85 km is 5×10^{-5} S/m for daytime and 3.5×10^{-6} S/m for nighttime, which are close to the values of *Rycroft et al.* [2008]. Our calculation shows that an electric field ($\mathbf{E}_{z=85}$) of ~ 1 mV/m at 85 km can be produced by current density $J_{\rm rock} = 1.4$ μA/m^2 for daytime conductivity, or by a current density of only $J_{\rm rock} = 0.1$ μA/m^2 for nighttime conductivity. The SAMI3 model is employed to simulate the ionosphere dynamics in the region above the lower boundary at 85 km. The electric field $\mathbf{E}_{z=85}$ is an input to the model and acts as a driving source in the electric potential equation.

[15] A schematic sketch of the electrical coupling between the ionosphere and the surface charges in the earthquake fault zone is shown in Figure 3. The surface charge distribution function in the earthquake fault zone is an input to our numerical simulations. Solved by current continuity equation [*Tzur and Roble*, 1985], $\nabla \cdot \mathbf{J} = \nabla \cdot (\boldsymbol{\sigma}\mathbf{E}) = 0$, the electric field is shown between two conducting planes – the ground ($z = 0$) and the bottom of the ionosphere (z = 85 km) . Here $\boldsymbol{J}$ is current and $\mathbf{E}$ is electric field, and $\boldsymbol{\sigma}$ is the conductivity tensor. The upward current (orange lines) is driven by the vertical upward electric field (red lines). The current flows toward the ionosphere partially in the horizontal direction and produces an outward electric field ($\mathbf{E}_{z=85}$) at an altitude of 85 km. It is further found that the electric fields and current density at z = 85 km, and resulting ionosphere dynamics are mainly determined by the telluric current density $J_{\rm rock}$, independent of Earth's surface conductivity.

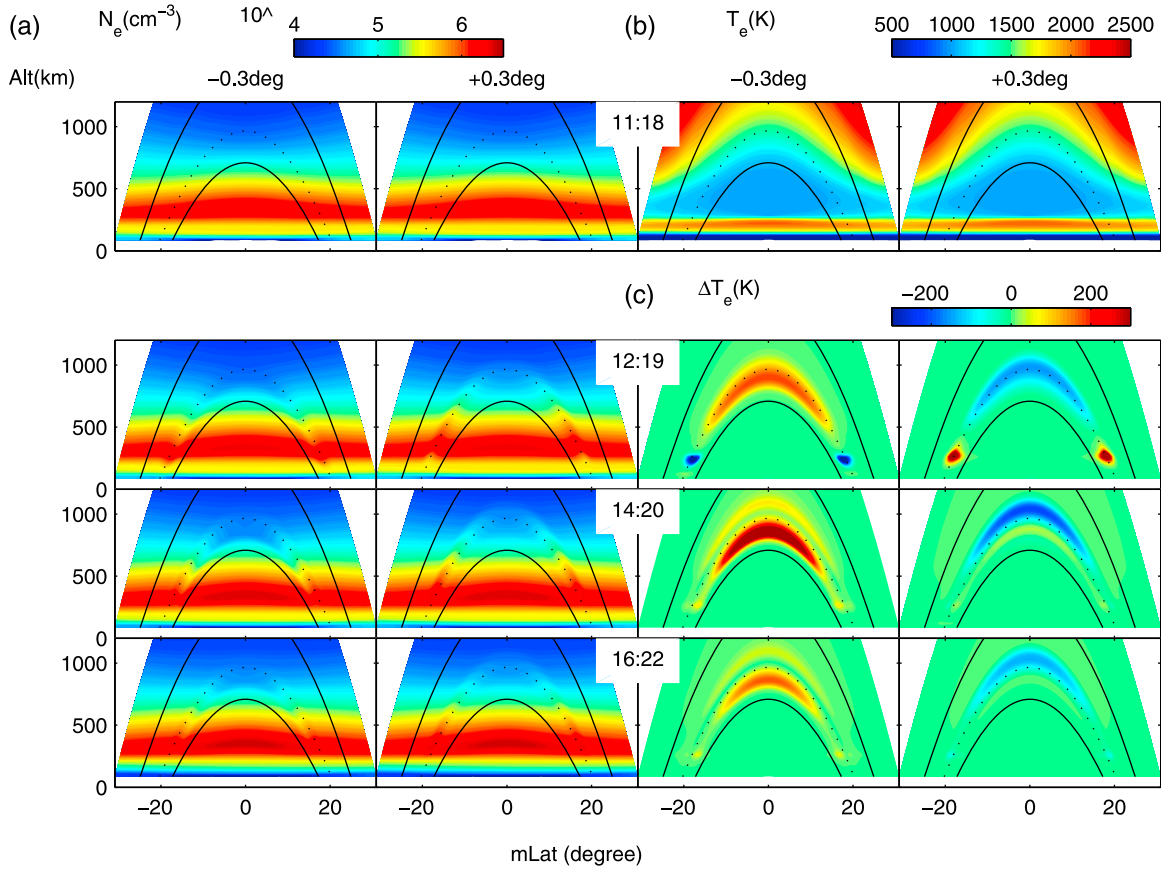

Figure 4. The simulations results for a daytime case with a current density of $J_{rock} = 3.0\ \mu A/m^2$: contour plots of (a) electron density, (b) electron temperature, and (c) temperature variations in two meridian planes with longitude −0.3° and 0.3°. The electric fields are switched on in the time period between LT 12 and 13. (top) At LT 11:18 (first row), contour plots of electron density and electron temperature before switch-on of electric field. At later times, the $\boldsymbol{E} \times \boldsymbol{B}$ drift motion reduces (enhances) the electron density, and increases (decreases) electron temperature in the −0.3° (0.3°) meridian plane.

[16] The NRL three-dimensional ionosphere simulation code SAMI3, including ion dynamics and electric potential, is used to investigate the TEC variations caused by the electric field from the surface charges of earthquake fault zone. We express the vector form of current continuity equation ($\nabla \cdot \mathbf{J} = 0$) in the ionosphere, in terms of dipolar coordinates (s, p, φ). The dipolar coordinates (s, p, φ) can be transferred from spherical polar coordinates (r, θ, φ) for Earth geographic system,

$$s = \frac{R_E^3}{r^2}\cos\theta \tag{13}$$

$$p = \frac{r}{R_E}\frac{1}{\sin^2\theta} \tag{14}$$

$$\varphi = \varphi \tag{15}$$

where R_E is Earth radius, $\theta = 0$ to π is for latitude −90 to 90 degree, and φ is longitude degree. We integrate equations (13)–(15) along the magnetic field from the base of southern hemisphere to the northern hemisphere. The integrated electric potential equation, derived from current conservation ($\nabla \cdot J = 0$) in dipolar coordinates (s, p, ϕ), is used in this study [*Huba et al.*, 2008, 2009a, 2009b, 2009c; *Krall et al.*, 2009a, 2009b],

$$\frac{\partial}{\partial p}p\Sigma_{pp}\frac{\partial\Phi}{\partial p} - \frac{\partial}{\partial p}\Sigma_h\frac{\partial\Phi}{\partial\phi} + \frac{\partial}{\partial\phi}\frac{1}{p}\Sigma_{p\phi}\frac{\partial\Phi}{\partial\phi} + \frac{\partial}{\partial\phi}\Sigma_h\frac{\partial\Phi}{\partial p} = \frac{\partial F_{pg}}{\partial p} + \frac{\partial F_{pV_n}}{\partial p} - \frac{\partial F_{pE_{ex}}}{\partial p} + \frac{\partial F_{\phi g}}{\partial\phi} + \frac{\partial F_{\phi V_n}}{\partial\phi} - \frac{\partial F_{\phi E_{ex}}}{\partial\phi} \tag{16}$$

where $\Sigma_{pp} = \int(p\Delta/b_s)\sigma_p ds$, $\Sigma_{p\phi} = \int(1/pb_s\Delta)\sigma_p ds$ and $\Sigma_H = \int(1/b_s)\sigma_h ds$; $F_{pg} = -\int r\sin\theta(B_0/c)\sigma_p g_p ds$, $F_{\phi g} = \int(r_E\sin^3\theta/\Delta)(B_0/c)\sigma_h g_p ds$, $F_{pVn} = \int r\sin\theta(B_0/c)(\sigma_p V_{n\phi} + \sigma_H V_{np})ds$, and $F_{\phi Vn} = \int(r_E\sin^3\theta/\Delta)(B_0/c)(\sigma_H V_{n\phi} - \sigma_P V_{np})ds$; g_p is the component of gravity perpendicular to B; V_{np} and $V_{n\phi}$ are perpendicular wind components; σ_p is the Pedersen conductivity, and σ_H is the Hall conductivity. The additional two source terms of external penetrated E-field (E_p, E_ϕ) are $F_{pEex} = \int r\sin\theta(\sigma_p E_{ex,p} + \sigma_h E_{ex,\varphi})ds$ and $F_{\varphi Eex} = \int\frac{R_E\sin^3\theta}{\Delta b_s}(\sigma_p E_{ex,\varphi} + \sigma_h E_{ex,p})ds$, respectively. The integrated electric potential in equation (16) is solved in the SAMI3 and the resulting electric field is used to self-consistently transport the plasma.

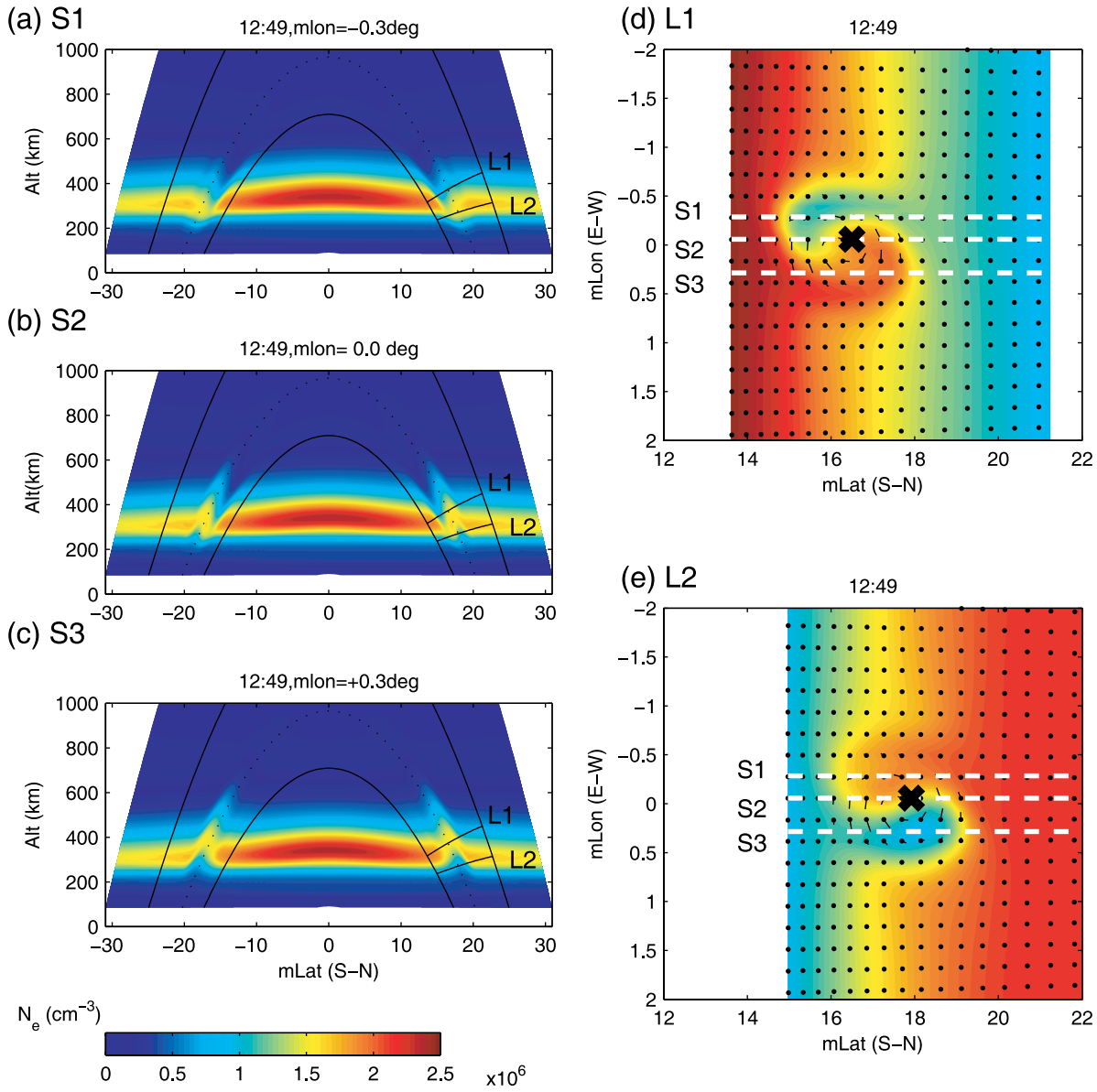

Figure 5. The modeling ionosphere electron density at time LT 12:49 in three meridian planes: (a) S1 with magnetic longitude −0.3°, (b) S2 with magnetic longitude 0.0°, and (c) S3 with magnetic longitude +0.3°. Also shown are (d) the electron density and plasma flow velocity in the L1 plane and (e) those in the L2 plane.

[17] In equation (16), the equal potential is assumed along the geomagnetic field line because the conductivity parallel to field line is much greater than conductivity perpendicular to field line. Hence, we solve the electric potential in two dimensional coordinates (p, φ). The external eclectic field can be transmitted along the field line.

4. Daytime Results

[18] Figure 4 shows the simulation results for a daytime case (J_{rock} = 3.0 μA/m^2) with external electric field ($\mathbf{E}_{z=85}$ = 2.1 mV/m), switched on at local time (LT) 12:00 to 13:00. To maintain the surface charges and electric field near ground, the currents from the stressed rock must be continuously supplied in the time period. Otherwise, the charges and associated electric fields will decay with a characteristic time 44 s for the conductivity $\sigma_{air} = 2 \times 10^{-13}$ Sm^{-1} or 440 s for the conductivity $\sigma_{air} = 2 \times 10^{-14}$ Sm^{-1}. The surface charges are distributed in a fault zone 200 km in the north-south direction and 30 km in the east-west direction, its orientation is north-south and centered at latitude 20° and longitude 0°, indicated by white dot in Figures 6b and 6c.

[19] The electron density and temperature at LT 11:18 (before the charge switch-on) are shown in Figure 4 (top). The density is horizontally stratified. Contour plots of the electron density and temperature variation in the meridional planes −0.3° (westward) and 0.3° (eastward) are shown in Figures 4a and 4c, respectively. The decrease (increase) of density on the top side of the ionosphere at −0.3° (+0.3°) and time LT 12:19 in Figure 4a is associated with the $\boldsymbol{E} \times \boldsymbol{B}$ motion (see Figure 3) of the plasma, bringing the lower

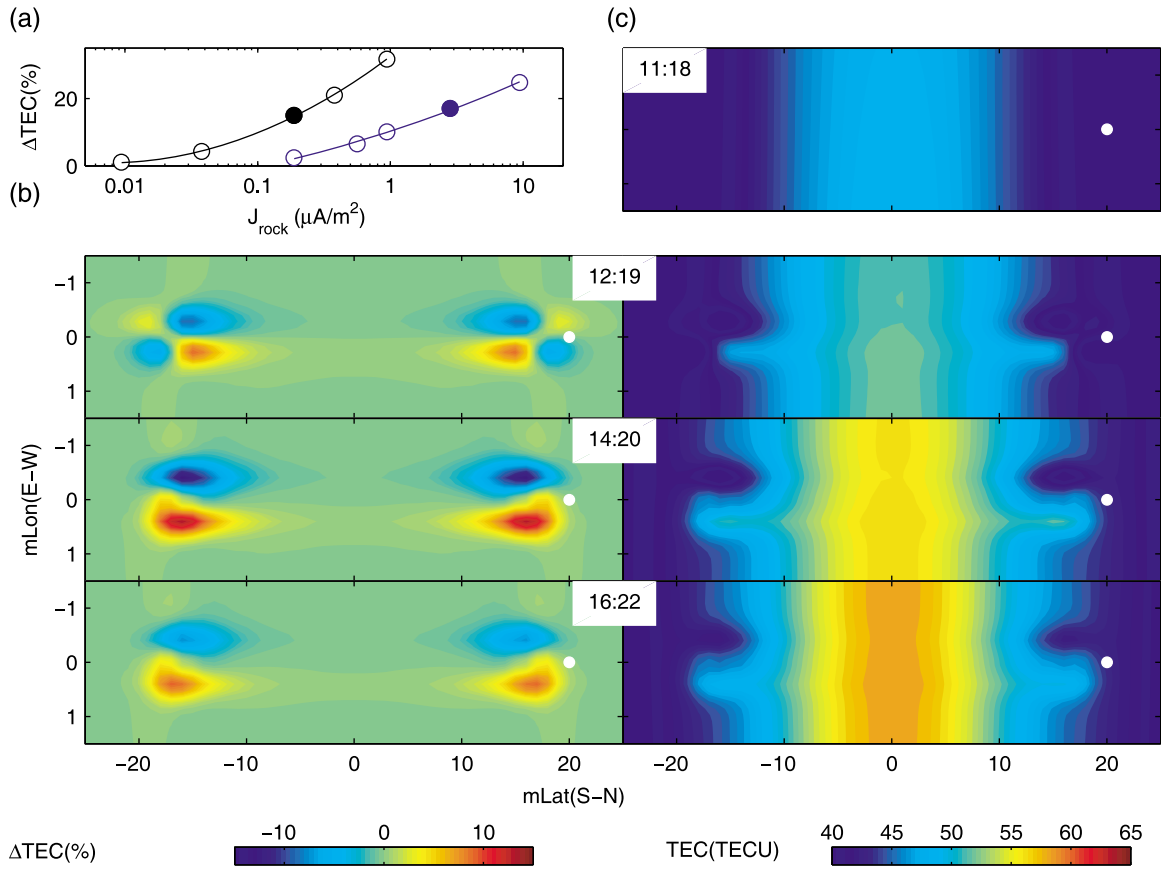

Figure 6. (a) ΔTEC, the percentage change of total electron content (TEC), as a function of current density J_{rock} in the earthquake fault region for the daytime ionosphere (blue line) with a larger conductivity and nighttime ionosphere (black line) with a lower conductivity. (b) Contour plots of ΔTEC and (c) contour plots of TEC in units of TECU (1 TECU = 10^{12} electron/cm^2) at different times for the case shown in Figure 4. The white dot indicates the location of earthquake fault.

(higher) density plasma downward (upward). Figure 4c shows the corresponding electron temperature variation (ΔT_e) which is anti-correlated with electron density variation. The electron temperature variations can be up to 100–250 K in the daytime ionosphere. This is also associated with the $\boldsymbol{E} \times \boldsymbol{B}$ motion of the plasma, which bring the hotter (cooler) electrons downward (upward). Although the perturbation (charge) is located at latitude 20°, the perturbed electric field can map to the conjugate region (−20°). The entire flux tube is affected by the charge at latitude 20° because of the assumption of equipotential field lines.

[20] Figure 5 shows a more detailed view of the $\boldsymbol{E} \times \boldsymbol{B}$ motion of plasma. The modeling ionosphere electron density at time LT 12:49 in three meridian planes is shown in Figure 5a for S1 with magnetic longitude −0.3 degree, Figure 5b for S2 with magnetic longitude 0.0 degree and Figure 5c for S3 with magnetic longitude +0.3 degree. The dashed line denotes the magnetic field line passing through the center of earthquake fault region (mLat 20°, mLon 0°) in the northern hemisphere. The solid lines perpendicular to dashed lines show the projecting lines for perpendicular planes, indicated by "L1" and "L2." In Figures 5d and 5e, the "L1" and "L2" planes perpendicular to the magnetic field lines show the electron density in linear color scale and $\boldsymbol{E} \times \boldsymbol{B}$ drift velocity in vectors.

[21] The plane "L1" above the ionospheric hmF_2 has higher (lower) electron density in the left (right) side of Figure 5d since the plane is tilted above hmF_2. The electric field radiates outward from the mapping earthquake epicenter where the epicenter is projected by a symbol of black cross in Figure 5d. The magnetic field is directed into the paper. Therefore, the $\boldsymbol{E} \times \boldsymbol{B}$ motion drives the plasma to rotate counterclockwise. In Figure 5d, the $\boldsymbol{E} \times \boldsymbol{B}$ drift of plasma cause the electron density enhancement on the east side (longitude degree > 0) of the mapping earthquake epicenter and electron density reduction on the west side (longitude degree < 0) of the epicenter. For the plane L2 tilted below the hmF_2, Figure 5e shows an electron density enhancement (reduction) on the west (east) side of the epicenter.

[22] Figure 6a shows the maximum TEC percentage change (ΔTEC) as a function of current densities J_{rock} from 0.2 to 10 μA/m^2 for daytime (blue lines). The corresponding maximum electric field at z = 85 km is 0.14–7.1 mV/m. The maximum ΔTEC is 2% to 25%. Figure 6b shows contour plots of ΔTEC, and Figure 6c shows TEC contour plots for the same case shown in Figures 4 and 5 with J_{rock} = 3.0 μA/m^2. The ΔTEC plots show a quadrupole pattern at LT 12:19 that later develops a dipolar pattern. The affected TEC region in the ionosphere is limited to ±0.5° in longitude. The orientation of fault has a minor effect on the magnitude of TEC variations

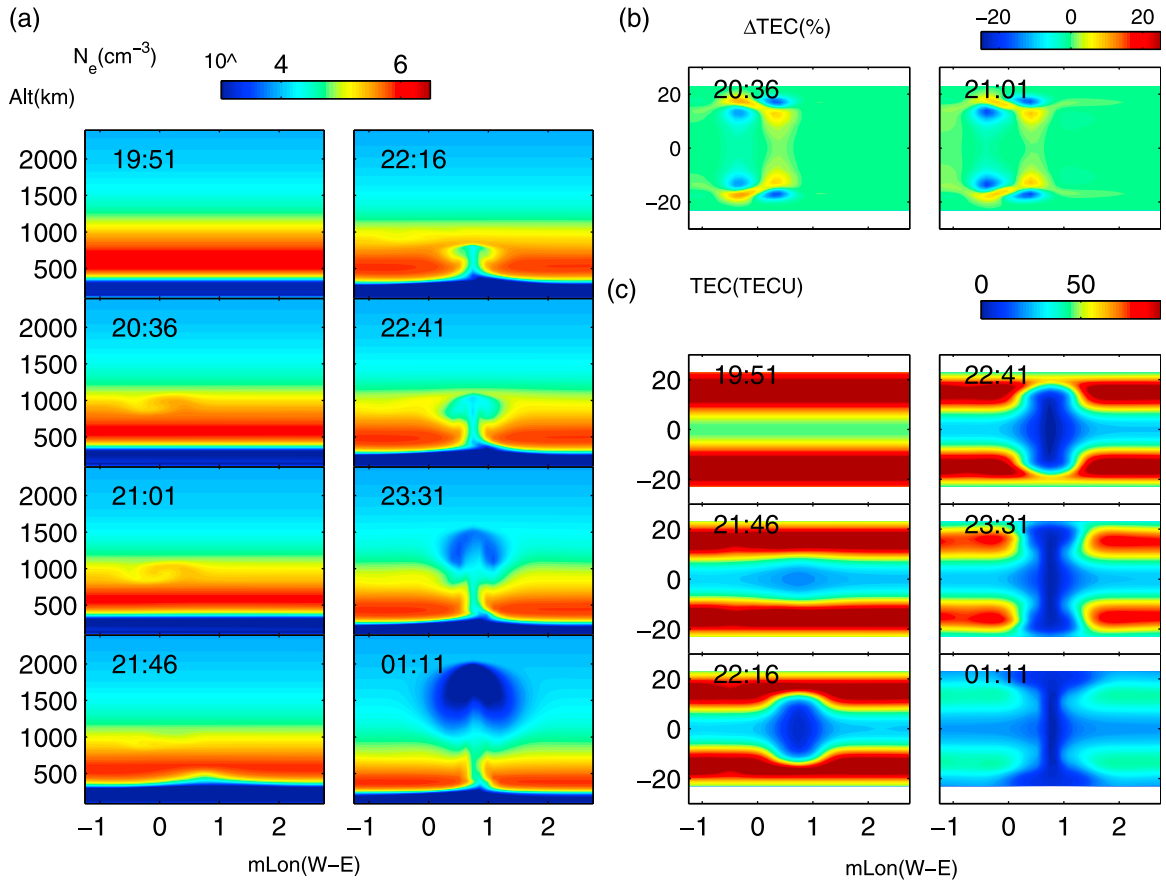

Figure 7. (a) Contour plots of electron density N_e in the equatorial plane at different times for the nighttime case with current density J_{rock} = 0.2 μA/m^2. The plasma vortex is formed at early time and plasma bubble at later time. (b) Contour plots of ΔTEC during formation of plasma vortex. (c) Contour plots of TEC during formation of plasma bubble.

because the external electric field $\mathbf{E}_{z=85}$ is on the same order for the same total surface charges of the earthquake fault zone with different orientation. Due to the inclination of geomagnetic field lines, the latitudinal range of the affected region depends on the location of the epicenter [*Pulinets and Boyarchuk*, 2004]. It is found that the affected region extends 1500 km, 1000 km, 600 km and 500 km from the epicenter in the equatorial direction for epicenter located at latitude 15°, 20°, 40° and 60°, respectively. Since the plasma density and peak altitude of the F2 region change with solar cycle, the affected region will also change with solar cycle.

5. Nighttime Results

[23] Figure 7 shows the results for the case in which a nighttime current density J_{rock} = 0.2 μA/m^2 in the earthquake fault zone is switched on from LT 20:00 to 21:00. The driven electric field at the bottom of ionosphere maps along the magnetic field to the equatorial plane, as illustrated in Figure 3. Figure 7a shows the contour plots of electron density at LT 20:36 and 21:01, and Figure 7b shows the corresponding ΔTEC contour plots. The maximum ΔTEC are about 15% at LT 20:36 and LT 21:01. Figure 7a also shows that, at LT 21:46, a plasma bubble is initiated at longitude 0.7 degree on the east side of meridional plane of surface charge center, where the $\boldsymbol{E} \times \boldsymbol{B}$ motion is upward as shown in Figure 3 and plasma depletion occurs below the F peak. The bubble reaches an altitude 900 km at LT 22:16, 1100 km at LT 22:41, 1600 km at LT 23:31 and 2000 km at LT 01:11. The corresponding TEC contour plots in Figure 7c illustrate that the plasma is first depleted in equator region, and the depleted region expands poleward. The width of plasma-depleted region is about 1 degree in longitude, its latitude range can extend to ±30 degree, and the height of plasma bubble can grow to 2000 km at LT 01:11. For a greater current density J_{rock} = 1.0 μA/m^2, the plasma bubble will be initiated at an earlier time (LT 21:41) due to a stronger upward $\boldsymbol{E} \times \boldsymbol{B}$ motion. We expect that the effect of a ground, pre-earthquake charge distribution on the ionosphere will be a function of latitude, longitude, and geophysical conditions (e.g., F10.7) because of the orientation of the geomagnetic field and ionospheric conditions.

[24] In our numerical experiments, there is no threshold for the rock current density to cause TEC variations. However, as shown in Figure 6a, a rock current density of J_{rock} = 0.5 μA/m^2 is required to cause 5% of TEC variations or ΔTEC = 5% for the daytime ionosphere. For the nighttime ionosphere, only a smaller current density of J_{rock} = 0.04 μA/m^2 is required to have ΔTEC = 5%. On the other hand, a minimum threshold of current density J_{rock} = 0.01 μA/m^2 is needed to trigger the formation of nighttime plasma bubble.

[25] The crustal deformation is generally a continuing process. As rock is continuously subjected to stress in the earthquake preparation period, the rock current density $J_{\rm rock}$ is generated, leading to TEC variations. However, the resulting TEC variations must be large enough to be detectable. Before the main shock, the stress may be increased to produce detectable TEC variations. After the main shock, part of stress is released and ionosphere effect becomes weak. The TEC variations are not necessary to occur within only one month before main shock. The magnitude of $J_{\rm rock}$ over the stressed rock is the key factor to affect the ionosphere.

6. Summary

[26] In summary, we have formulated a coupling model for the stressed rocks-Earth surface charges-atmosphere-ionosphere system. We have also proposed a model for the build-up of surface charges over the stressed rock and in the nearby air based on the experimental results by *Freund et al.* [2009] and *Freund* [2010]. We then calculated the electric fields and currents in the atmosphere and simulated the ionospheric response. The main results can be summarized as follows.

[27] 1. As rocks are subjected to stress, rocks can activate hole ($h^{\bullet}$) charge carriers and generate electric currents along stress-gradient, causing the accumulation of positive charges at the earth surface. The surface charges consist of positive charges at the rock surface and charged O_2^+ ions from field-ionization in the air. The injection of positively charged air ions at the rock-to-air interface will produce a vertical electric field $\boldsymbol{E}_{air}$, which in turn drives an upward current, J_{air}, removing part of the surface charges. When the inflow rock current J_{rock} is balanced by the outflow current J_{air}, the total surface charge Q reaches an asymptotic value Q_∞.

[28] 2. The air conductivity $\sigma_{\rm air}$ above the pre-earthquake zone is highly enhanced due to the injection of airborne positive ions associated with the telluric current $J_{\rm rock}$.

[29] 3. Our study shows that the magnitude of current density $J_{\rm rock}$ is the most important parameter to determine the TEC variations and nighttime bubble formation in the ionosphere.

[30] 4. The simulation results show that the current density $J_{\rm rock}$ = 0.2–10 μA/m^2 in the earthquake fault zone can cause TEC variations of up to 2–25% in daytime ionosphere.

[31] 5. The simulation results also show that a current density $J_{\rm rock}$ = 0.01–1 μA/m^2 can lead to nighttime TEC variations of 1–30% as well as the formation of a nighttime plasma bubble (equatorial spread F) extending over the whole magnetic flux tube containing the earthquake epicenter.

[32] 6. We suggest that observations of daytime and nighttime TEC variations and nighttime plasma bubbles within the affected region can be used as precursors for earthquake prediction.

[33] **Acknowledgments.** We are grateful to the National Center for High-performance Computing in Taiwan and Center for Computational Geophysics in National Central University for computer time and facilities. This work of CLK and LCL was supported in part by grants (NSC 98-2111-M-008-001, NSC 099-2811-M-006-004, NSC 100-2811-M-006-004, NSC 99-2111-M-006-001-MY3) from National Science Council in Taiwan. The research of JDH and GJ was supported by the Office of Naval Research (ONR). We are also thankful for insightful discussions with F. Freund, J. Y. Liu, and M. Q. Chen.

[34] Robert Lysak thanks Friedemann Freund and another reviewer for their assistance in evaluating this paper.

References

Bhattacharya, S., S. Sarkar, A. K. Gwal, and M. Parrot (2009), Electric and magnetic field perturbations recorded by DEMETER satellite before seismic events of the 17th July 2006 M 7.7 earthquake in Indonesia, *J. Asian Earth Sci.*, *34*(5), 634–644, doi:10.1016/j.jseaes.2008.08.010.

Bolt, B. A. (2004), *Earthquakes*, 5th ed., 378 pp., W. H. Freeman, New York.

Chuo, Y. J., Y. I. Chen, J. Y. Liu, and S. A. Pulinets (2001), Ionospheric foF2 variations prior to strong earthquakes in Taiwan area, *Adv. Space Res.*, *27*(6–7), 1305–1310, doi:10.1016/S0273-1177(01)00209-5.

Cole, R. K., Jr., and E. T. Pierce (1965), Electrification in the Earth's atmosphere for altitudes between 0 and 100 kilometers, *J. Geophys. Res.*, *70*, 2735–2749, doi:10.1029/JZ070i012p02735.

Davies, K., and D. M. Baker (1965), Ionospheric effects observed around the time of the Alaskan earthquake of March 28, 1964, *J. Geophys. Res.*, *70*, 2251–2253, doi:10.1029/JZ070i009p02251.

Foppiano, A. J., E. M. Ovalle, K. Bataille, and M. Stepanova (2008), Ionospheric evidence of the May 1960 earthquake over Concepción?, *Geofis. Int.*, *47*(3), 179–183.

Freund, F. (2000), Time-resolved study of charge generation and propagation in igneous rocks, *J. Geophys. Res.*, *105*, 11,001–11,019, doi:10.1029/1999JB900423.

Freund, F. (2002), Charge generation and propagation in igneous rocks, *J. Geodyn.*, *33*, 543–570, doi:10.1016/S0264-3707(02)00015-7.

Freund, F. (2010), Toward a unified solid state theory for pre-earthquake signals, *Acta Geophys.*, *58*(5), 719–766, doi:10.2478/s11600-009-0066-x.

Freund, F., and D. Sornette (2007), Electro-magnetic earthquake bursts and critical rupture of peroxy bond networks in rocks, *Tectonophysics*, *431*, 33–47, doi:10.1016/j.tecto.2006.05.032.

Freund, F. T., I. G. Kulahci, G. Cyr, J. Ling, M. Winnick, J. Tregloan-Reed, and M. M. Freund (2009), Air ionization at rock surfaces and pre-earthquake signals, *J. Atmos. Sol. Terr. Phys.*, *71*, 1824–1834, doi:10.1016/j.jastp.2009.07.013.

Geller, R. J. (1997), Earthquake prediction: A critical review, *Geophys. J. Int.*, *131*, 425–450, doi:10.1111/j.1365-246X.1997.tb06588.x.

Huba, J. D., G. Joyce, and J. Krall (2008), Three-dimensional equatorial spread F modeling, *Geophys. Res. Lett.*, *35*, L10102, doi:10.1029/2008GL033509.

Huba, J. D., G. Joyce, J. Krall, and J. Fedder (2009a), Ion and electron temperature evolution during equatorial spread F, *Geophys. Res. Lett.*, *36*, L15102, doi:10.1029/2009GL038872.

Huba, J. D., J. Krall, and G. Joyce (2009b), Atomic and molecular ion dynamics during equatorial spread F, *Geophys. Res. Lett.*, *36*, L10106, doi:10.1029/2009GL037675.

Huba, J. D., S. L. Ossakow, G. Joyce, J. Krall, and S. L. England (2009c), Three-dimensional equatorial spread F modeling: Zonal neutral wind effects, *Geophys. Res. Lett.*, *36*, L19106, doi:10.1029/2009GL040284.

Kanamori, H. (2003), Earthquake prediction: An overview, in *Academic*, edited by W. H. K. Lee et al., pp. 1205–1216, Academic, San Diego.

Krall, J., J. D. Huba, G. Joyce, and S. T. Zalesak (2009a), Three-dimensional simulation of equatorial spread-F with meridional wind effects, *Ann. Geophys.*, *27*, 1821–1830, doi:10.5194/angeo-27-1821-2009.

Krall, J., J. D. Huba, and C. R. Martinis (2009b), Three-dimensional modeling of equatorial spread F airglow enhancements, *Geophys. Res. Lett.*, *36*, L10103, doi:10.1029/2009GL038441.

Liu, J. Y., Y. I. Chen, S. A. Pulinets, Y. B. Tsai, and Y. J. Chuo (2000), Seismo-ionospheric signatures prior to M>=6.0 Taiwan earthquakes, *Geophys. Res. Lett.*, *27*, 3113–3116, doi:10.1029/2000GL011395.

Liu, J. Y., Y. I. Chen, Y. J. Chuo, and H. F. Tsai (2001), Variations of ionospheric total electron content during the Chi-Chi earthquake, *Geophys. Res. Lett.*, *28*, 1383–1386, doi:10.1029/2000GL012511.

Liu, J. Y., et al. (2009), Seismo-ionospheric GPS total electron content anomalies observed before the 12 May 2008 M_w7.9 Wenchuan earthquake, *J. Geophys. Res.*, *114*, A04320, doi:10.1029/2008JA013698.

Moore, G. W. (1964), Magnetic disturbances preceding the 1964 Alaska earthquake, *Nature*, *203*(4944), 508–509, doi:10.1038/203508b0.

Park, S. K., M. J. S. Johnston, T. R. Madden, F. D. Morgan, and H. F. Morrison (1993), Electromagnetic precursors to earthquakes in the ULF band: A review of observations and mechanisms, *Rev. Geophys.*, *31*(2), 117–132, doi:10.1029/93RG00820.

Parrot, M., J. Achache, J. J. Berthelier, E. Blanc, A. Deschamps, F. Lefeuvre, M. Menvielle, J. L. Plantet, P. Tarits, and J. P. Villain (1993), High-frequency seismo-electromagnetic effects, *Phys. Earth Planet. Inter.*, *77*(1–2), 65–83, doi:10.1016/0031-9201(93)90034-7.

Pulinets, S., and K. Boyarchuk (2004), *Ionospheric Precursors of Earthquakes*, 315 pp., Springer, Berlin.

Pulinets, S. A., K. A. Boyarchuk, V. V. Hegai, V. P. Kim, and A. M. Lomonosov (2000), Quasielectrostatic model of atmosphere-thermosphere-ionosphere coupling, *Adv. Space Res.*, *26*(8), 1209–1218, doi:10.1016/S0273-1177(99)01223-5.

Pulinets, S. A., A. D. Legen'ka, T. V. Gaivoronskaya, and V. K. Depuev (2003), Main phenomenological features of ionospheric precursors of strong earthquakes, *J. Atmos. Sol. Terr. Phys.*, *65*, 1337–1347, doi:10.1016/j.jastp.2003.07.011.

Riousset, J. A., V. P. Pasko, and A. Bourdon (2010), Air-density-dependent model for analysis of air heating associated with streamers, leaders, and transient luminous events, *J. Geophys. Res.*, *115*, A12321, doi:10.1029/2010JA015918.

Rycroft, M., R. Harrison, K. Nicoll, and E. Mareev (2008), An overview of Earth's global electric circuit and atmospheric conductivity, *Space Sci. Rev.*, *137*, 83–105, doi:10.1007/s11214-008-9368-6.

Scholz, C. H., L. R. Sykes, and Y. P. Aggarwal (1973), Earthquake prediction: A physical basis, *Science*, *181*, 803–810, doi:10.1126/science.181.4102.803.

Silina, A. S., E. V. Liperovskaya, V. A. Liperovsky, and C. V. Meister (2001), Ionospheric phenomena before strong earthquakes, *Nat. Hazards Earth Syst. Sci.*, *1*(3), 113–118, doi:10.5194/nhess-1-113-2001.

Toutain, J.-P., and J.-C. Baubron (1999), Gas geochemistry and seismotectonics: A review, *Tectonophysics*, *304*, 1–27, doi:10.1016/S0040-1951(98)00295-9.

Tzur, I., and R. G. Roble (1985), The interaction of a dipolar thunderstorm with its global electrical environment, *J. Geophys. Res.*, *90*, 5989–5999, doi:10.1029/JD090iD04p05989.

Zhao, B., M. Wang, T. Yu, W. Wan, J. Lei, L. Liu, and B. Ning (2008), Is an unusual large enhancement of ionospheric electron density linked with the 2008 great Wenchuan earthquake?, *J. Geophys. Res.*, *113*, A11304, doi:10.1029/2008JA013613.

J. D. Huba, Plasma Physics Division, Naval Research Laboratory, Washington, DC 20375, USA.

G. Joyce, Icarus Research, Inc., PO Box 30780, Bethesda, MD 20824, USA.

C. L. Kuo and L. C. Lee, Institute of Space Science, National Central University, Jhongli 32001, Taiwan. (loulee@jupiter.ss.ncu.edu.tw)